Received: 12 June 2025 | Revised: 31 July 2025 | Accepted: 5 August 2025

DOI: 10.1111/ijac.70047

International Journal of Applied Ceramic Technology
Ceramic Product Development and Commercialization

SPECIAL ISSUE ARTICLE

# Highly dense translucent $CeO_{2-\delta}\cdot(RE, Y, Sm, La)_2O_3$ (RE = Dy, Gd) high-entropy ceramics for multi-wavelength emission

**Avnee Chauhan**[1,2] | **Andreas Frickel**[2] | **Sabine Begand**[2] | **Mathias Herrmann**[3] | **Enrico Bernardo**[4] | **Dušan Galusek**[1,5]

[1]Centre for Functional and Surface Functionalized Glass, Alexander Dubček University of Trenčín, Trenčín, Slovakia

[2]Fraunhofer Institute for Ceramic Technologies and Systems, Hermsdorf, Germany

[3]Fraunhofer Institute for Ceramic Technologies and Systems, Dresden, Germany

[4]Department of Industrial Engineering, Università Degli Studi di Padova, Padova, Italy

[5]Joint Glass Centre of the IIC SAS, TnUAD and FChPT STU, Trenčín, Slovakia

**Correspondence**
Avnee Chauhan and Dušan Galusek, Centre for Functional and Surface Functionalized Glass, Alexander Dubček University of Trenčín, Študentská 2, Trenčín 911 50, Slovakia.
Email: avnee.chauhan@tnuni.sk; dusan.galusek@tnuni.sk

**Editor's Choice**
The Editor-in-Chief recommends this outstanding article.

**Funding information**
APVV, Grant/Award Number: 23-0424

**Abstract**

This study reports the synthesis of translucent, high-entropy oxide (HEO) ceramics with the composition $CeO_{2-\delta}\cdot(RE, La, Sm, Y)_2O_3$ (RE = Dy, Gd), and a single-phase bixbyite structure (space group Ia-3). The materials were prepared by reactive sintering at 1600°C in air, achieving translucency through optimized ball milling of precursor oxides and refinement of processing parameters. X-ray diffraction and scanning electron microscopy confirmed phase purity and a highly dense microstructure, with relative densities exceeding 99%. The samples were translucent in the visible and near-infrared part of the spectrum. To improve the transparency, hot isostatic pressing (HIP) at 1600°C and 185 MPa was employed on the samples sintered for 6 h. HIP induced partial phase separation, impairing translucency. The effect of dwell time on luminescence properties of reactive sintered samples was also studied. Ultraviolet–visible spectroscopy revealed a narrower bandgap and an enhanced photoluminescence (PL) intensity in the sample sintered for 6 h, as a result of a higher concentration of oxygen vacancies. PL under 302 nm excitation displayed multi-wavelength emissions peaking at 432, 572, and 653 nm, producing near-cold white light. Time-resolved PL decay analysis indicated multiple luminescence centers with efficient energy transfer (e.g., $Ce^{3+}$ to $Sm^{3+}/Dy^{3+}/Gd^{3+}$).

**KEYWORDS**
ball milling, high-entropy ceramic, optical properties, translucency, white light application

## 1 | INTRODUCTION

In the quest for sustainable development and energy-efficient technologies, the field of optics has seen a relentless drive toward discovering advanced materials. Among these materials, rare-earth oxides have gathered significant attention due to their exceptional properties, positioning them as superior alternatives to traditional materials

---

*Int J Appl Ceram Technol.* 2025;22:e70047.
https://doi.org/10.1111/ijac.70047

such as fluoride and lithium-based glasses for various optical applications.[1–4] These oxides exhibit outstanding thermal and chemical stability, nonlinear refraction, and high quantum yield, making them invaluable in modern high-tech optical industries.

Recently, high-entropy oxides (HEOs) are gaining attention for optical applications. These materials are stabilized by the high entropy of mixing of multiple principal elements, leading to unique structural and functional properties.[5] Lattice distortion in HEOs induces new functional properties, thereby expanding their potential applications.[6] HEOs have demonstrated the applicability of HEOs in manufacturing innovative optoelectronic devices, photocatalytic systems, thermal imaging, optical probes, and plasma display panels.[7] Due to their wide bandgap, high-entropy rare-earth oxides are promising candidates for various applications, including laser hosts, scintillating devices, multi-wavelength phosphors, and luminescent materials.[8,9] These materials have been explored for use in ultraviolet (UV) light emitting diode (LED)-pumped solid-state white light generation, wide-band white light emission, white LEDs, red and orange light emission, green light emission, solid-state lighting devices, various types of lasers, UV LEDs, nonlinear optical devices, near-infrared (NIR) luminescence, optoelectronics, optical fiber amplification, active and passive optical fibers, optical displays, and multifunctional luminescence applications.[10,11]

In addition to these applications, high-entropy ceramics were fabricated in a transparent form, thus further contributing to the field of optics. Optical transparency in HEOs is vital for applications involving white light, such as LEDs and lighting, where efficient transmission of the full visible spectrum enhances brightness and color quality. With their wide bandgaps and stability, HEOs enable durable, transparent layers for white light devices, optoelectronics, and protective coatings.

In 2019, Chen and Wu reported the first high-entropy transparent fluoride ceramics, with a composition of $CeNdCaSrBaF_{12}$ introducing transparency as a new property of high-entropy ceramics.[8] Zhang et al. reported preparation of high-entropy transparent $(La_{0.2}Nd_{0.2}Sm_{0.2}Gd_{0.2}Yb_{0.2})_2Zr_2O_7$ oxide ceramics. This ceramic material was fabricated by vacuum sintering and contained mixed fluorite deficient and ordered pyrochlore phases.[12] In other studies, Zhang et al. fabricated $(Lu_{0.2}Gd_{0.2}Y_{0.2}Yb_{0.2}Dy_{0.2})_2O_3$ and $(Lu_{0.2}Y_{0.395}Gd_{0.2}Yb_{0.2}Tm_{0.05})_2O_3$ high-entropy transparent sesquioxide ceramics by vacuum sintering.[13,14] The latter was the first reported optical functional high-entropy ceramic material to show up-conversion properties. Up-conversion emission from the $Tm^{3+}$ ion at 485 nm was observed upon laser emission excitation at 980 nm, resulting from cooperative energy transfer from $Yb^{3+}$ to $Tm^{3+}$ ions. Recent studies further highlight the optical versatility of HEOs. For instance, $(La_{0.2}Lu_{0.2}Y_{0.2}Gd_{0.2}Ce_{0.2})AlO_3$ ceramics showed 405 nm emission by $Gd^{3+}$ to $Ce^{3+}$ energy transfer under 286.5 nm excitation, indicating potential for high-energy conversion.[15] Similarly, $(La_{0.2}Dy_{0.2}Er_{0.2}Yb_{0.2}Y_{0.2})_2Zr_2O_7$ exhibited pressure-sensitive photoluminescence (PL), suggesting applications in optical sensing.[16] Transparent $(Gd_{0.2}Tb_{0.2}Y_{0.2}Lu_{0.2}Yb_{0.2})_3Al_5O_{12}$ ceramics, synthesized by co-precipitation and spark plasma sintering, achieved 74% transmittance at 3.6 µm with $Tb^{3+}$ and $Yb^{3+}$ up-conversion emissions.[17] $(Y_{0.2}La_{0.2}Gd_{0.2}Eu_{0.2}Er_{0.2})_2O_3$ nanoceramics, prepared by thermobaric treatment, reached 70% visible transparency and a 51% luminescence quantum yield, surpassing traditional $Y_2O_3$:Eu phosphors.[18] Perovskite $RNiO_3$ (R = La, Pr, Nd, Sm, Eu) medium-entropy thin films demonstrated enhanced transparency and 2.3 S/cm p-type conductivity, making them ideal candidate for flexible electrodes. LTZSHGNGO ceramics, with a cubic pyrochlore structure, achieved a high dielectric constant (~1680 at 650°C) due to the presence of oxygen vacancies, suggesting broader multifunctional applications.[19]

In our previous study, high-entropy (Ce, RE)$O_{2-\delta}$·(La, Sm, Y)$_2O_3$ (RE = Pr) and $CeO_{2-\delta}$·(RE, La, Sm, Y)$_2O_3$ (RE = Gd, Dy) were synthesized to investigate the effect of elemental substitution on optical properties. The presence of Pr in mixed oxidation states ($Pr^{3+}/Pr^{4+}$) influenced energy transfer mechanisms and emission characteristics. Replacing Pr with Gd or Dy significantly widened the bandgap and altered luminescence behavior.[20]

Present study focuses on achieving highly dense translucent HEOs with the composition $CeO_{2-\delta}$·(RE, La, Sm, Y)$_2O_3$ (RE = Gd, Dy), achieved through reactive sintering at 1600°C in air and hot isostatic pressing (HIP). Unlike the opaque samples (~97% density) reported previously,[20] the process optimization yielded >99% relative density, achieving translucency in the prepared HEO system. By leveraging $Ce^{3+}/Ce^{4+}$ mixed valence, oxygen vacancies and rare-earth ion transitions, finetuning of bandgap and white light emission is achieved, surpassing luminescence outputs reported previously. The optimization of optical properties paves way to tailoring optical characteristics of HEO ceramics.

## 2 | EXPERIMENTAL PROCEDURE

### 2.1 | Powder processing and sample preparation

High-purity oxides, yttrium(III) oxide ($Y_2O_3$; 99% purity; Leuchtstoffwerke Breitungen GmbH [LWB]), lanthanum(III) oxide ($La_2O_3$; 99.9%; LWB), cerium(IV) oxide

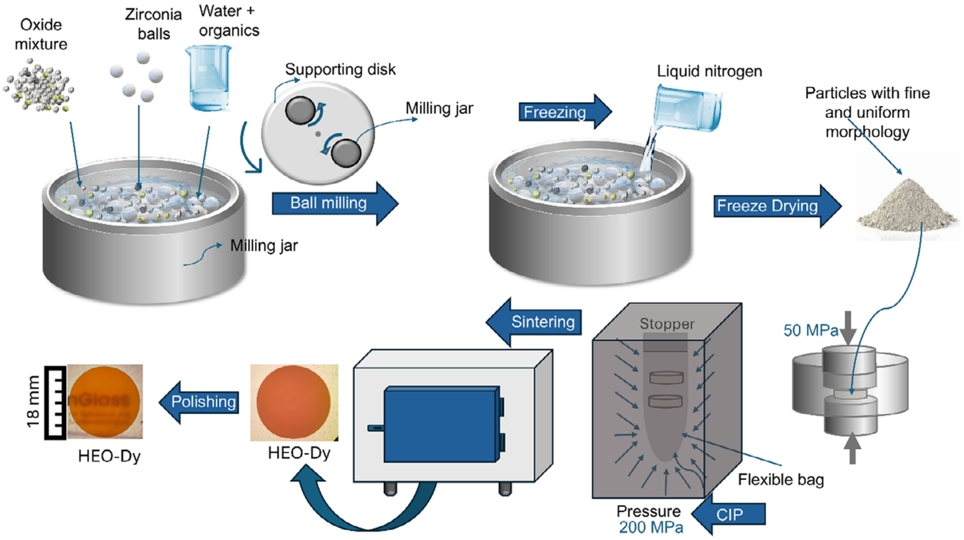

**FIGURE 1** Schematic of the process applied for the preparation of the high-entropy oxide ceramics in this study.

($CeO_2$; 99%; LWB), samarium(III) oxide ($Sm_2O_3$; 99.9%; LWB), and dysprosium(III) oxide ($Dy_2O_3$; 99.9%; LWB), were used as raw materials for the HEO preparation. Dolapix CE64 (Zschimmer & Schwarz) was used as dispersant and glycine as pressing aid. All the chemicals were analytical reagent grade and were used as received without further purification.

To synthesize HEOs, the binary oxides were weighed individually according to their stoichiometric ratio to achieve an equimolar cation mixture. Deionized water and organic dispersants were added to the mixture to facilitate uniform suspension and prevent agglomeration. The powders were homogenized using a planetary ball mill with 1 mm zirconia milling balls at 250 rpm for 60 min. After removing the milling media, glycerin was added under continuous stirring. The slurry was then rapidly solidified using liquid nitrogen and subsequently dried in a freeze dryer to eliminate any residual moisture without causing agglomeration. The powder was sieved through a 50 µm mesh sieve.

Cylindrical pellets for sintering experiments were prepared by uniaxial pressing of the powder at 50 MPa in a 20 mm diameter die and subsequently cold isostatically pressed at 200 MPa to increase density and handling strength. Burn-out of organic additives was completed by gradually heating the pellets to 600°C at a rate of 0.5 K/min, holding for 3 h, and cooling at 3 K/min. The pellets were sintered under precisely defined conditions: heating at 0.5 K/min up to 650°C, 2 K/min up to 1600°C, isothermal dwell at 1600°C for 2, 6, or 10 h, and cooling down to room temperature at 5 K/min.

The pellets sintered for 6 h were HIPed at 1600°C/185 MPa at a heating rate of 3 K/min, dwell time of 8 h, and then cooled at 2 K/min to eliminate any remaining porosity. Finally, the pellets were annealed for 4 h at 1000°C in air to relieve any residual stress and stabilize the crystal structure. The synthesis procedure is outlined in Figure 1. The sintered samples were cut into smaller pieces that were mounted in a polymeric resin and polished using diamond abrasive disks to obtain polished cross-sections for microstructure examination and to outline the grain boundaries. Grain boundaries were visualized by thermal etching in the air. The samples were heated to 1500°C at a rate of ±5 K/min and held at this temperature for 1 h.

## 2.2 | Characterization

The particle size distribution of oxide powders in the ball-milled suspensions was evaluated by dynamic light scattering analysis using LS 13 320 Laser Diffraction Particle Size Analyzer Instrument (Beckman Coulter, Inc.) The polycrystalline nature of sintered samples was confirmed by X-ray powder diffraction using an X-ray diffractometer (Bruker, D8 Advance), with Cu K$\alpha$ radiation in an angular range $10° < 2\theta < 80°$ with a step size of 0.01°. Particle morphology of ball-milled powders and microstructure of sintered ceramics were examined using a field emission gun scanning electron microscope (Zeiss, ultra 55 plus). Elemental distribution was analyzed using EDAX Octane Elect Super-System (SSD), EDAX APEX advanced-software electron microscope equipped with energy-dispersive X-ray detector. The information on the oxidation state of elements was obtained by X-ray photoelectron spectroscopy (XPS). A Thermo-Scientific Nexsa

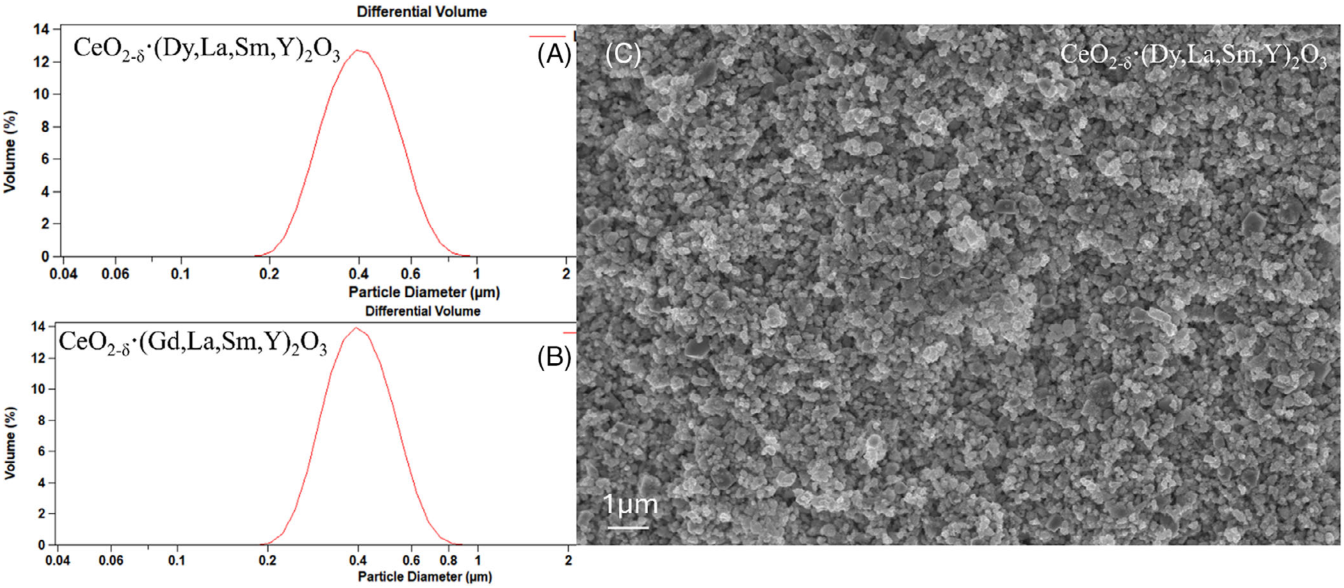

**FIGURE 2** (A and B) Particle size distribution of mixed oxide powders used as precursors for the preparation of high-entropy oxide powders after ball milling. (C) Scanning electron microscopy (SEM) micrograph of the mixed oxide powders used to prepare $CeO_{2-\delta}\cdot$(Dy, La, Sm, Y)$_2$O$_3$ after milling.

G2 instrument was used, employing Al K$\alpha$ radiation with a 400 µm spot size as an X-ray source. The analyzer's pass energy was fixed to 50 eV with a 1.0 eV step size to obtain general spectra for $CeO_{2-\delta}\cdot$(RE, La, Sm, Y)$_2$O$_3$ (RE = Dy, Gd) sintered samples. A Cary 5000 spectrometer (Agilent) was used to record the UV–visible–NIR (UV–Vis–NIR) absorption spectra of the prepared HEOs in the wavelength range from 200 to 2000 nm. The optical bandgaps were determined from the obtained UV–Vis spectra using the Tauc relation plot.

$$[F(R_\infty)\cdot h\nu]^{1/n} = A\left(h\nu - E_g\right) \tag{1}$$

The Kubelka–Munk function, $F(R_\infty)$ was used, where $A$ is a constant, $h$ represents Planck's constant, $\nu$ is the vibrational frequency, and $E_g$ is the bandgap energy. The exponent $n$ implies the nature of the optical transitions, with $n = 1/2$ and 2 indicating the allowed direct and indirect transitions, respectively. The bandgap values (both direct and indirect) were calculated at the inflection point of Tauc's plots, using linear regression. The intercept of the fitted straight line with the $h\nu$ axis was taken as the bandgap value. The PL excitation and emission spectra were measured using a Fluorolog FL3-2l spectrometer (Horiba). A photomultiplier tube detector R928 (Hamamatsu Photonics K.K.) was used in the spectrometer in photon counting mode. A 450 W Xenon-lamp was used as an excitation light source. Cut-off filters were employed in all measurements to eliminate the second-order diffraction of the radiation source on the grating.

## 3 | RESULTS AND DISCUSSION

### 3.1 | Particle size prior to shaping and sintering

The particle size distribution of mixed oxide powders after ball milling is shown in Figure 2A,B. The distribution of particle size was unimodal, and the mean particle size was measured to be less than ~1 µm. This value was lower than the initial powder's particle size, indicating effective reduction of particle size by milling. The scanning electron microscopy (SEM) micrographs confirmed the particle size distribution of the ball-milled powders, as depicted in Figure 2C. The optimized milling parameters yielded powders with uniform particles, and equiaxed morphology.

### 3.2 | Phase formation and microstructural homogeneity

The crystal structure formation and stability of HEOs were investigated by X-ray powder diffraction after sintering the $CeO_{2-\delta}\cdot$(RE, La, Sm, Y)$_2$O$_3$ (RE = Dy, Gd) powders at 1600°C with isothermal holding times of 2, 6, and 10 h. X-ray diffraction (XRD) confirmed that all the samples

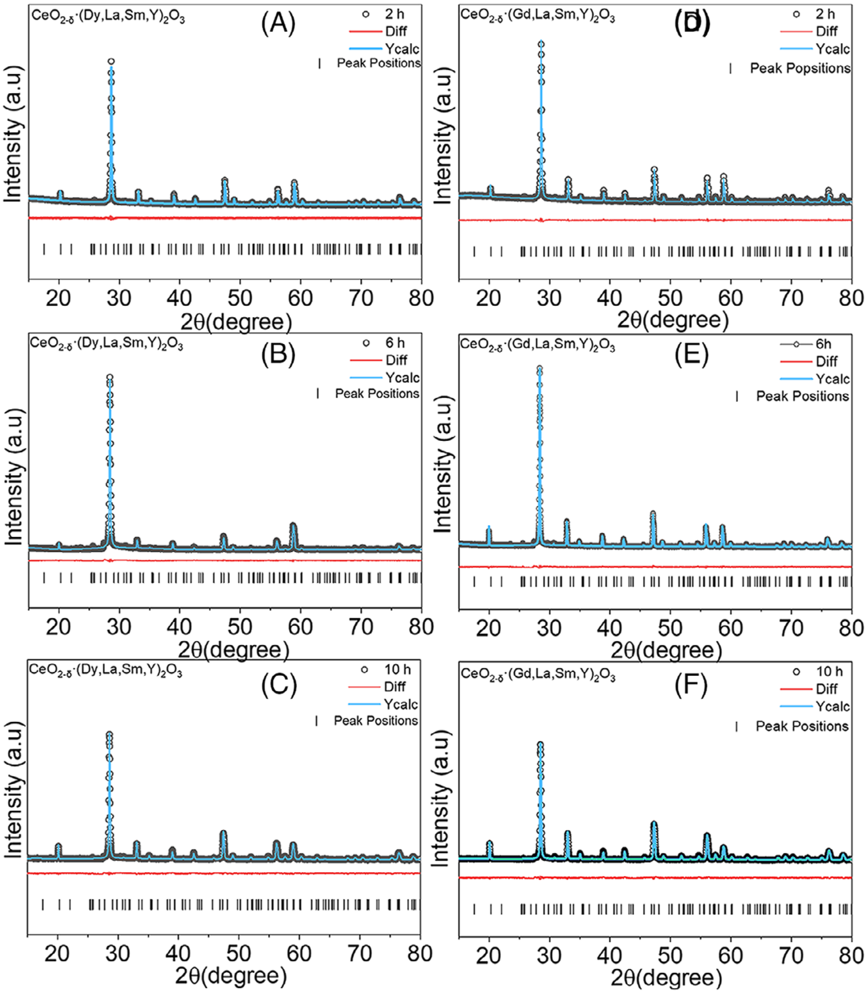

**FIGURE 3** (a–f) X-ray diffraction (XRD) patterns of $CeO_{2-\delta}$·(RE, La, Sm, Y)$_2O_3$ (RE = Gd, Dy) ceramics sintered for 2, 6, and 10 h at 1600°C.

contained a single-phase with bixbyite structure, and the space group Ia-3 (Figure 3A–F). The investigated materials contained Ce, Y, Sm, La, Dy, and Gd cations. All considered cations are characterized by similar ionic radii and predominantly exist in the $RE^{3+}$ oxidation state, except for cerium, which exhibits both $Ce^{3+}$ and $Ce^{4+}$ states. As practically all used ions exhibit a high mutual solubility,[21,22] it can be expected they would form a single-phase solid solution.

The full width half maximum (FWHM) of the diffraction maxima are narrow, indicating well developed crystals. However, variations in the intensities of the diffraction maxima corresponding to (111) and (222) planes of some samples were observed. This could potentially arise from texture effects, where crystallites align isotropically during sintering, or form oxygen vacancies altering the scattering factors of these planes. Compared to our previous work,[20] the superlattice peaks in the XRD patterns are more pronounced and exhibit higher intensity, indicating more pronounced oxygen vacancy ordering with the peaks vanishing when ordering is lost.

Rietveld refinement of the XRD data was performed to precisely determine the structural parameters, including the lattice parameters, theoretical density, measured density, and phase purity: the results are summarized in Table 1. The refinement studies confirmed that the five rare-earth cations were homogeneously distributed in a single-phase bixbyite structure, with no secondary phases of individual rare-earth oxides detected.

Black vertical lines in Figure 3 correspond to the reflection positions of $Sm_2O_3$ (PDF-01-076-7403). While the single-phase nature of bixbyite structure was preserved for all dwell times of sintering, variations in the lattice parameter and bulk density were observed. The slight reduction in the FWHM of the diffractions reflects improved homogeneity and a larger crystal size related to the grain growth. The density increased incrementally due to enhanced densification and microstructure consolidation with time. Optimization of pressing and sintering parameters increased the relative density from 97% achieved under the conditions reported in our previous work[20] (uniaxial pressing at 50 MPa and sintering at

**TABLE 1** Rietveld refinement parameters of $CeO_{2-\delta}\cdot(Dy, La, Sm, Y)_2O_3$ powder, Rietveld refinement factor ($R_{wp}$, $S$), lattice constant ($a$), unit cell volume ($V$), theoretical density ($\rho_T$), measured density ($\rho$), numbers in parentheses indicate standard deviations for the last digit(s) of lattice constant ($a$), and unit cell volume ($V$).

| Sample | Time (h) | $R_{wp}$ | $S$ | $a$ (Å) | $V$ (∀$^3$) | $\rho_T$ (g/cm$^3$) | $\rho$ (g/cm$^3$) |
|---|---|---|---|---|---|---|---|
| $CeO_{2-\delta}\cdot(Dy, La, Sm, Y)_2O_3$ | 2 | 5.44 | 3.05 | 10.88 (15) | 1290 (5) | 6.61 | 6.57 |
| | 6 | 7.21 | 5.58 | 10.88 (3) | 1290 (11) | 6.61 | 6.59 |
| | 10 | 4.79 | 2.64 | 10.87 (2) | 1285 (7) | 6.64 | 6.63 |
| $CeO_{2-\delta}\cdot(Gd, La, Sm, Y)_2O_3$ | 2 | 5.11 | 2.92 | 10.92 (14) | 1303 (5) | 6.51 | 6.48 |
| | 6 | 3.74 | 2.04 | 10.92 (9) | 1302 (3) | 6.56 | 6.54 |
| | 10 | 4.82 | 2.56 | 10.90 (2) | 1296 (7) | 6.55 | 6.55 |

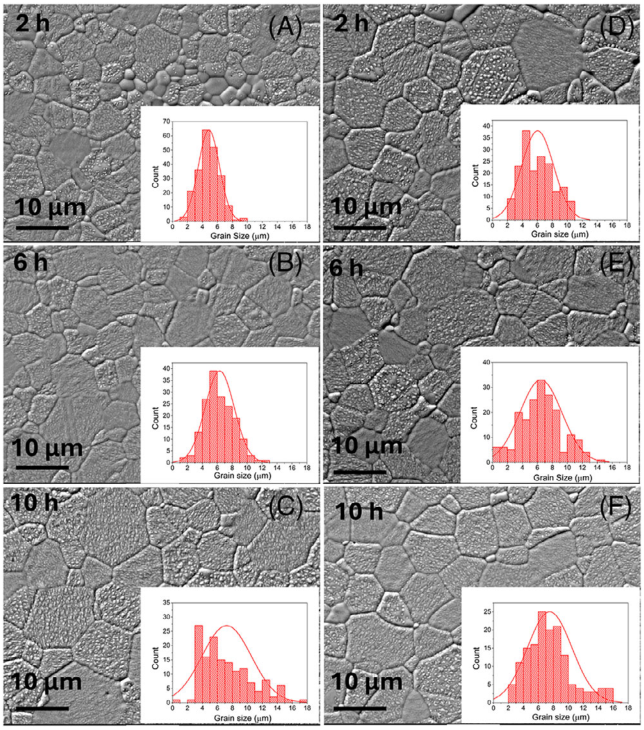

**FIGURE 4** Microstructure and grain size distribution of high-entropy oxide (HEO) ceramics: (A–C) $CeO_{2-\delta}\cdot(Dy, La, Sm, Y)_2O_3$ and (D–F) $CeO_{2-\delta}\cdot(Gd, La, Sm, Y)_2O_3$ sintered at 1600°C for 2, 6, and 10 h, respectively.

1450°C–1550°C for 10 h) to over 99% (uniaxial pressing at 50 MPa, combined with subsequent cold isostatic pressing at 200 MPa, and sintering at 1600°C with controlled heating rates and dwell times of 2–10 h). The near theoretical density may be also related to the observed changes in the (111) and (222) plane diffraction intensities and the stronger superlattice peaks, reflecting improved structural order and vacancy organization.

The microstructure homogeneity of the HEOs samples $CeO_{2-\delta}\cdot(RE, La, Sm, Y)_2O_3$ (RE = Gd, Dy) sintered at 1600°C for 2, 6, and 10 h was examined by SEM. The results are shown in Figure 4. The samples were cut and polished for cross-sectional SEM analysis, revealing a dense microstructure with no visible micro-voids, confirming high densifications for all times of sintering. The grain size distribution was relatively uniform (shown in the inset), with an average grain size ranging from 5 to 10 µm. Only a minimal variation of grain size between the samples sintered for 2 h and those sintered for 10 h was observed, suggesting that the time of isothermal dwell during sintering had only a limited impact on the grain growth under the applied conditions. Energy-dispersive X-ray spectroscopy (EDX) analysis was performed to examine the elemental distribution within the HEOs $CeO_{2-\delta}\cdot(RE, La, Sm, Y)_2O_3$ (RE = Gd, Dy) sintered at 1600°C for 2, 6, and 10 h. Table 2 shows atomic percentage of all elements in HEOs, confirming nearly equimolar ratios of all rare-earth elements.

The $CeO_{2-\delta}\cdot(Dy, La, Sm, Y)_2O_3$ composition sintered at 1600°C for 6 h was further processed by HIP at 1600°C and 185 MPa for 8 h under Ar atmosphere to enhance the optical transparency of the material.

XRD (shown in Figure 5) confirmed the presence of single-phase bixbyite structure (space group Ia-3, $a = 10.85$ Å), which was the only crystalline phase detected in $CeO_{2-\delta}\cdot(RE, La, Sm, Y)_2O_3$ (RE = Dy, Gd) HEOs after sintering at 1600°C. The high intensity and the small width of the (222) diffraction at $2\theta = 28.50°$ suggests the presence of some large crystals. All major diffractions of bixbyite are also present, albeit at much lower intensity than expected from the respective powder diffraction file. After HIPing at 1600°C and 185 MPa for 8 h, a Ce-rich $RE_2O_3$ phase ($a = 10.98$ Å) emerged as a minor phase, with slightly shifted diffraction maxima (marked with asterisk) in Figure 5. Annealing the HIPed sample at 1200°C in air did not affect phase separation, likely because limited cation diffusion at this temperature preserved the Ce-rich $RE_2O_3$ phase alongside the primary bixbyite structure.

The HIP-treated sample exhibited a highly dense microstructure, consistent with the near-theoretical density (>99% relative density; Figure 6A,B). EDX (Figure 6C–H) revealed that cerium (Ce) exhibited notable segregation with EDX maps showing larger cations,

**TABLE 2** Atomic percentage of various elements in the synthesized high-entropy oxides obtained by energy-dispersive X-ray spectroscopy analysis.

| Sample | Sintering time at 1600°C (h) | Element (at%) | | | | | |
|---|---|---|---|---|---|---|---|
| | | O | Ce | La | Sm | Y | Dy |
| $CeO_{2-\delta}$·(Dy, La, Sm, $Y)_2O_3$ | 2 | 60 | 6.2 ± 0.3 | 6.9 ± 0.6 | 7.2 ± 0.3 | 7.4 ± 0.6 | 7.3 ± 0.3 |
| | 6 | 60 | 8.1 ± 0.6 | 8.7 ± 0.7 | 7.8 ± 0.3 | 7.9 ± 0.7 | 7.4 ± 0.8 |
| | 10 | 60 | 8.2 ± 0.6 | 8.7 ± 0.8 | 8.2 ± 0.5 | 7.4 ± 0.5 | 7.6 ± 0.4 |
| | | O | Ce | La | Sm | Y | Gd |
| $CeO_{2-\delta}$·(Gd, La, Sm, $Y)_2O_3$ | 2 | 60 | 6.1 ± 0.5 | 8.6 ± 0.8 | 8.7 ± 0.6 | 8.0 ± 0.9 | 8.6 ± 0.4 |
| | 6 | 60 | 6.4 ± 0.5 | 8.6 ± 0.6 | 8.8 ± 0.6 | 7.9 ± 0.2 | 8.3 ± 0.7 |
| | 10 | 60 | 7.7 ± 0.4 | 8.6 ± 0.7 | 7.9 ± 0.5 | 8.1 ± 0.6 | 7.7 ± 0.6 |

*Note*: The content of oxygen was assumed to be constant, and equal to stoichiometric amount of oxygen in the material.

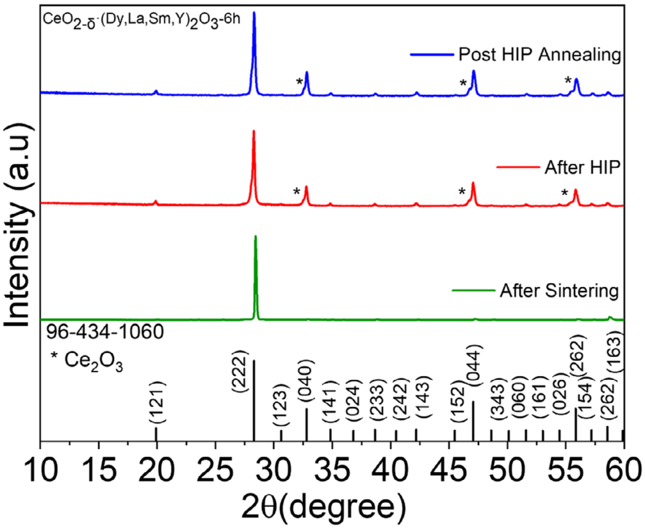

**FIGURE 5** X-ray diffraction (XRD) patterns of ceramics of $CeO_{2-\delta}$·(Dy, La, Sm, $Y)_2O_3$ sintered for 6 h at 1600°C and hot isostatic pressing (HIP) 1600°C and 185 MPa for 8 h and post-HIP annealing at 1000°C for 4 h in air.

especially La, in the Ce-segregated regions. However, Sm, Dy, and Y were depleted in the Ce-rich zones, indicating a size-dependent segregation mechanism where larger cations (Ce, La) separate from smaller ones (e.g., Y, Dy). The observed segregation suggests formation of localized secondary phases (possibly $RE_2O_3$) but the predominantly single-phase HEO with bixbyite structure was still retained. Some residual porosity was also observed, likely attributed to the change of Ce valence state changes ($Ce^{3+}/Ce^{4+}$) or defect stabilization during HIP, possibly influenced by trace impurities in the inert Ar atmosphere, which hindered complete densification. While the grain structure remained relatively uniform, the HIP treatment did not significantly enhance density of the material beyond the near-optimal state achieved during solid-state sintering step.

## 3.3 | Chemical analysis

XPS was employed to analyze the oxidation states of rare-earth cations and the chemical environment in $CeO_{2-\delta}$·(RE, La, Sm, $Y)_2O_3$ (RE = Gd, Dy) HEOs sintered at various dwell times. The high-resolution Ce 3d spectrum was deconvoluted into 10 distinct peaks corresponding to $Ce^{3+}$ and $Ce^{4+}$ oxidation state, as shown in Figures 7A and 8A.[23] The peaks corresponding to the binding energies of 916.8, 909.3, 901.2, 898.6, 889.7, and 882.4 eV are associated with the Ce $^3d_{5/2}$ and $^3d_{3/2}$ of $Ce^{3+}$, while the peaks observed at 904.3, 899.4, 885.7, and 880.3 eV correspond to the Ce $^3d_{5/2}$ and $^3d_{3/2}$ states of $Ce^{4+}$, respectively.[23,24]

The presence of $Ce^{4+}$ (peaks at 904.3, 899.4, 885.7, and 880.3 eV for Ce $^3d_{5/2}$ and $^3d_{3/2}$) alongside $Ce^{3+}$ (peaks at 916.8, 909.3, 901.2, 898.6, 889.7, and 882.4 eV) suggests that additional $O^{2-}$ ions are incorporated into the bixbyite structure (Ia-3) compared to a pure $M_2O_3$ lattice, likely filling some of the ordered oxygen vacancies inherent to the bixbyite structure, resembling the behavior of $CeO_2$–$Ce_2O_3$ solid solutions.

The La 3d spectra exhibited two distinct doublets, at around 834 and 850 eV, confirming the presence of $La^{3+}$, consistent with reported literature results (Figures 7B and 8B).[25] Similarly, the wide scan of Sm 3d XPS spectra shown in Figures 7C and 8C depicts characteristics of spin–orbital splitting peaks. The peak centered at 1110 and 1080 eV were assigned to $Sm^{3+}$ $^3d_{5/2}$ and $Sm^{3+}$ $^3d_{3/2}$, respectively, confirming the presence of samarium in the +3 oxidation states.[26] For yttrium (Figures 7D and 8D), the Y 3d scan (Figure 7D) located peaks at the binding energies of 160 and 158 eV, corresponding to $Y^{3+}$ $^3d_{3/2}$ and $Y^{3+}$ $^3d_{5/2}$, respectively, confirming the trivalent state of yttrium.[27]

The wide scan of $Dy^{3+}$ showed two prominent peaks at binding energies of $^3d_{3/2}$ (1335 eV) and $^3d_{5/2}$ (1299 eV) with an energy separation of 23 eV confirming the presence of $Dy^{3+}$ (Figure 7E). The Gd 4d spectrum exhibited a principal peak at 141.8 eV.[28] The wide shape of the

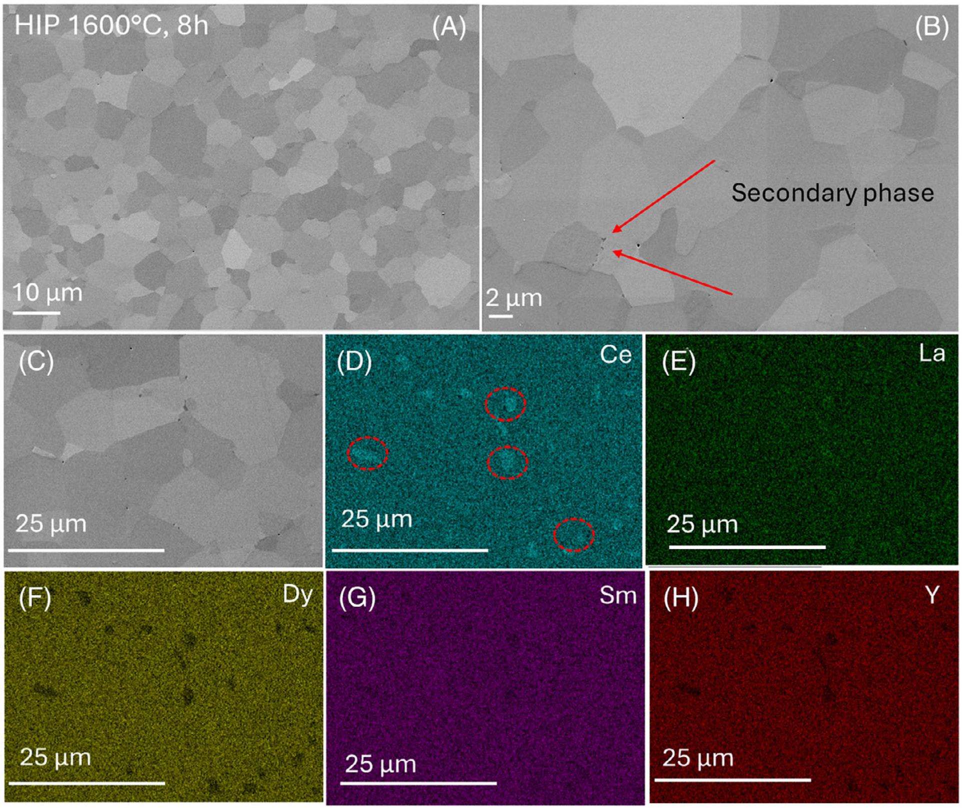

**FIGURE 6** Microstructure (A and B) and elemental distribution (C–H) of ceramics $CeO_{2-\delta}$·(Dy, La, Sm, Y)$_2O_3$ sintered for 6 h at 1600°C and subsequently hot isostatic pressed (HIPed) at 1600°C/185 MPa/8 h.

spectrum, spanning 30 eV, is attributed to strong 4d–4f Coulomb exchange interactions and spin–orbit coupling, confirming the presence of $Gd^{3+}$ in the structure shown in Figure 8E. The O 1s high-resolution spectrum was deconvoluted into three peaks labeled as $O_3$, $O_2$, and $O_1$. The $O_1$ peak at 529.6 eV corresponds to lattice oxygen (M–O bond), while the $O_2$ peak at 531.4 eV is associated with under-coordinated oxygen atoms or oxygen vacancies within the lattice, and the $O_3$ peak at 532.3 eV is attributed to surface-adsorbed oxygen species.

The presence of oxygen vacancies, as indicated by the $O_2$ peak, further corroborates the reduction of $Ce^{4+}$ to $Ce^{3+}$, while the relative intensity of lattice oxygen ($O_1$) suggests additional $O^{2-}$ incorporation due to $Ce^{4+}$, consistent with a $CeO_2$-like environment within the bixbyite lattice (Figures 7F and 8F). Overall, the XPS analysis confirmed homogeneous distribution of the rare-earth cations (Ce, La, Sm, Y, Dy, Gd) within the ceramic matrix, with no evidence of secondary phases or significant segregation. All expected peaks of the constituent cations are present and match their binding energies in the matrix.

From the area ratio between $Ce^{3+}$ and $Ce^{4+}$, and from the ratio between $O_2$ and $O_1$ shown in Table 3, it can be concluded that the content of oxygen vacancies increased for both compositions when the dwell time of sintering increased from 2 to 6 h. Despite sintering in air, the increase in the concentration of oxygen vacancies with the increase of sintering time from 2 to 6 h, is attributed to the grain growth, which reduced the grain boundary area, thus limiting oxygen incorporation from the atmosphere and favoring reduction $Ce^{4+}$ to $Ce^{3+}$.[29,30] In HEO systems, the formation of oxygen vacancies is energetically favored at high temperatures as compared to pure $CeO_2$ due to the presence of multiple rare-earth cations (Ce,

**TABLE 3** Comparison of changes in X-ray photoelectron spectroscopy peak area ratios of $Ce^{3+}$ to $Ce^{4+}$ and $O_2$ to $O_1$.

| HEO sample | $Ce^{3+}/Ce^{4+}$ ratio | $O_2/O_1$ ratio |
|---|---|---|
| Dy 2 h | 0.19 | 0.27 |
| Dy 6 h | 1.05 | 3.95 |
| Dy 10 h | 0.54 | 0.66 |
| Gd 2 h | 0.32 | 0.47 |
| Gd 6 h | 1.98 | 2.78 |
| Dy 10 h | 0.64 | 0.61 |

Abbreviation: HEO, high-entropy oxide.

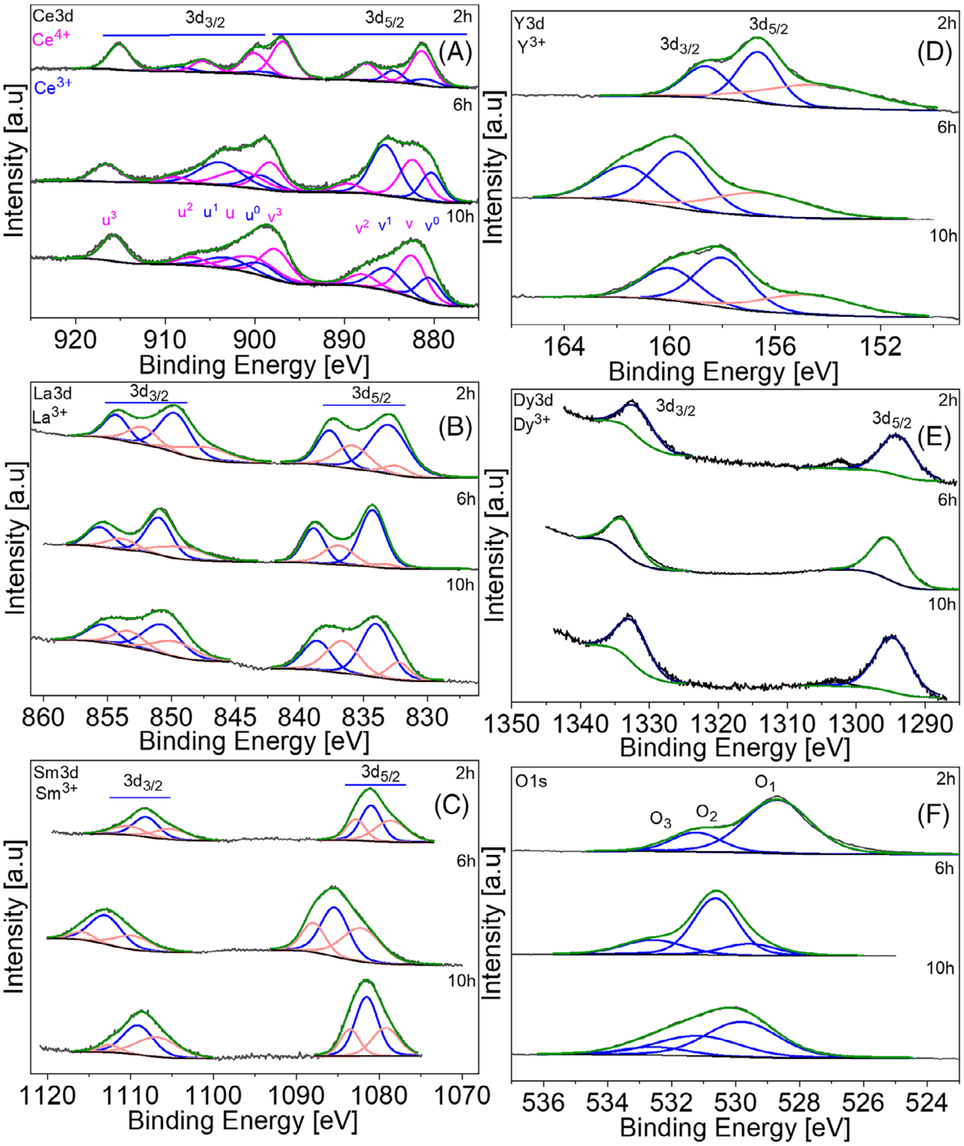

**FIGURE 7** High-resolution X-ray photoelectron spectroscopy (XPS) spectra of sintered high-entropy oxides (HEOs) at 1600°C for 2, 6, and 10 h, $CeO_{2-\delta}\cdot(Dy, La, Sm, Y)_2O_3$: (A) Ce 3d, (B) La 3d, (C) Sm 3d, (D) Y 3d, (E) Dy 3d, and (F) O 1s.

Gd/Dy, La, Sm, Y), which lowers the energy of formation of the vacancies.[31] In the present work, Ce in synthesized HEO ceramic originated from its oxide $CeO_2$, where Ce is present in the 4+ state. Open porosity in the green body allows oxygen access during early stages of sintering, maintaining a significant fraction of $Ce^{4+}$ after 2 h. From 2 to 6 h, reduced grain boundary area and high temperatures promoted the reduction of $Ce^{4+}$ to $Ce^{3+}$, increasing the concentration of oxygen vacancies. From 6 to 10 h, prolonged exposure to air enables oxygen diffusion into the bulk, oxidizing $Ce^{3+}$ to $Ce^{4+}$ and reducing oxygen vacancy concentration, as shown by the decreased $Ce^{3+}/Ce^{4+}$ and $O_2/O_1$ ratios in both compositions. The XPS results correlate with XRD data (Figure 3). The decreased intensities of diffractions corresponding to (111) and (222) planes with the increase of sintering time from 2 to 6 h reflect increased concentration of oxygen vacancies, which enhanced lattice disorder. Increased intensities of these diffractions with the increase of sintering time from 6 to 10 h indicated reduced amounts of vacancies concentrations and improved lattice ordering.

## 3.4 | Optical properties

UV–Vis spectroscopy was employed to estimate the bandgap of the single-phase $CeO_{2-\delta}\cdot(RE, La, Sm, Y)_2O_3$ (RE = Dy, Gd) HEOs sintered with the dwell times of 2, 6, and 10 h. Tauc plots, derived from the absorption spectra, were used to determine indirect and direct bandgap

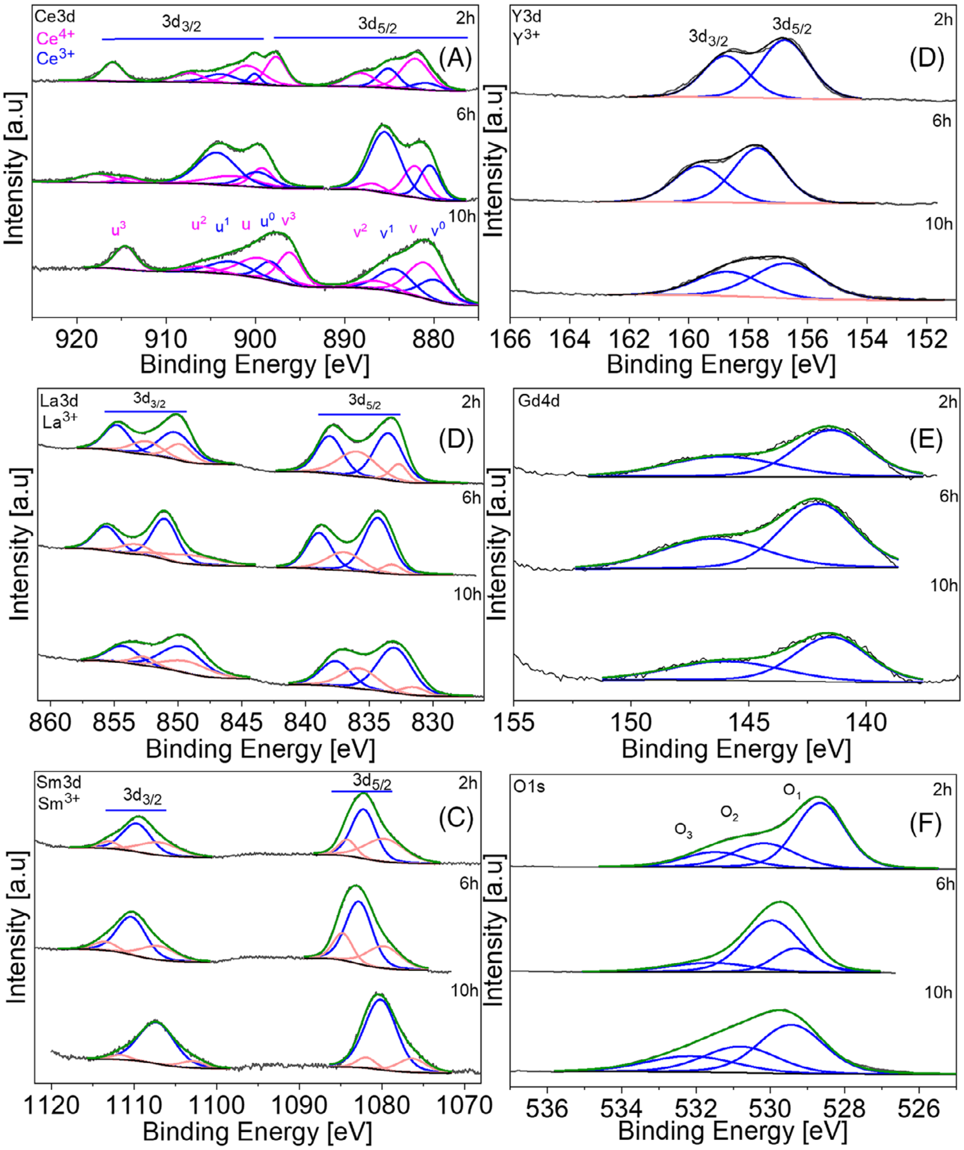

**FIGURE 8** High-resolution X-ray photoelectron spectroscopy (XPS) spectra of sintered high-entropy oxides (HEOs) at 1600°C for 2, 6, and 10 h, CeO$_{2-\delta}$·(Gd, La, Sm, Y)$_2$O$_3$: (A) Ce 3d, (B) La 3d, (C) Sm 3d, (D) Y 3d, (E) Gd 4d, and (F) O 1s.

energies, as shown in Figure 9A,B for CeO$_{2-\delta}$·(Dy, La, Sm, Y)$_2$O$_3$ and Figure 9C,D for CeO$_{2-\delta}$·(Dy, La, Sm, Y)$_2$O$_3$. The direct and indirect bandgap energy values for both compositions are summarized in Table 4, revealing distinct trends related to the sintering time. Samples sintered for 6 h exhibited the lower bandgap energy values compared to those sintered for 2 and 10 h, a trend confirmed by XPS data showing an increased oxygen vacancy concentration after 6 h of sintering.

**TABLE 4** Bandgap values of CeO$_{2-\delta}$·(Dy, La, Sm, Y)$_2$O$_3$ (RE = Dy, Gd).

| Sample name | Indirect bandgap (eV) | Direct bandgap (eV) |
|---|---|---|
| HEO-Dy 2 h | 2.15 | 2.65 |
| HEO-Dy 6 h | 2.12 | 2.57 |
| HEO-Dy 10 h | 2.14 | 2.61 |
| HEO-Gd 2 h | 2.36 | 2.79 |
| HEO-Gd 6 h | 2.33 | 2.75 |
| HEO-Gd 10 h | 2.35 | 2.78 |

Abbreviation: HEO, high-entropy oxide.

The formation and variation of oxygen vacancy concentration directly influence the bandgap energy; the reduction of bandgap energy is attributed to metastable states introduced by oxygen vacancies and Ce$^{3+}$/Ce$^{4+}$ mixed valence.[32,33] The high-entropy configuration featuring rare-earth elements (Gd, Dy, La, Sm, Y) with diverse ionic radii (e.g., Gd$^{3+}$:0.94 Å, Dy$^{3+}$:0.91 Å vs. Ce$^{4+}$:0.87 Å) and electronegativities further narrows the bandgap by

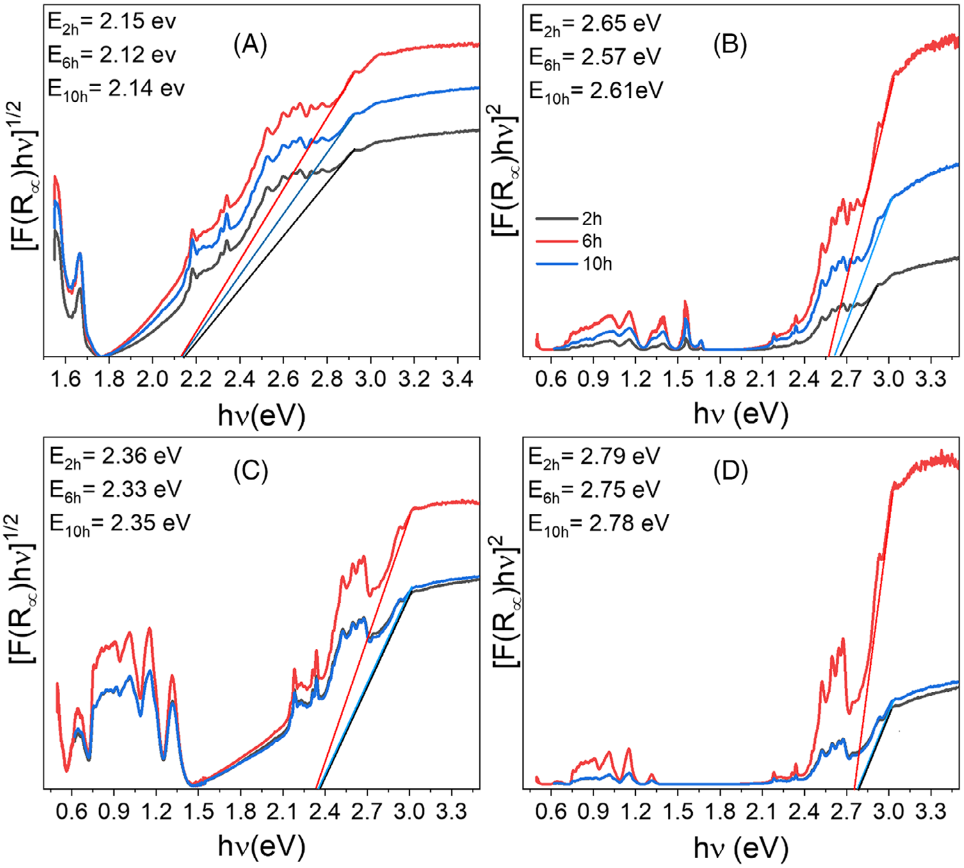

**FIGURE 9** (A) Indirect bandgap, (B) direct bandgap of $CeO_{2-\delta}\cdot(Dy, La, Sm, Y)_2O_3$, (C) indirect bandgap, and (D) direct bandgap of $CeO_{2-\delta}\cdot(Gd, La, Sm, Y)_2O_3$.

increasing lattice distortion and orbital overlap, dispersing the conduction and valence bands. This interplay of oxygen vacancies, cationic redox, and multi-element entropy effects underscore the tunability of fluorite-HEOs' optical properties, with optimized sintering at 6 h maximizing visible light emissions for applications such as white light emission and optoelectronics.[34]

To investigate the optical emission characteristics of the synthesized $CeO_{2-\delta}\cdot(RE, La, Sm, Y)_2O_3$ (RE = Gd, Dy) HEOs sintered at dwell times of 2, 6, and 10 h the PL spectra were recorded (Figure 10). The emission spectra reveal broad excitation and emission bands spanning the UV–Vis–NIR range driven by the luminescent transitions of $Ce^{3+}$, $Sm^{3+}$, $Dy^{3+}$, and $Gd^{3+}$ ions within bixbyite structured matrix. Figure 10A,B depicting the excitation spectra monitored at an emission wavelength of 615 nm featuring a peak at 302 nm, attributed to the $Ce^{3+}$, $^2F_{5/2} \rightarrow {}^5d_1$ transition, with corresponding emission spectra exhibiting broad visible peaks at 432 nm (blue) and 653 nm (red, likely involving $Sm^{3+}$), confirming multi-wavelength luminescence.

Down-conversion PL, under 302 nm excitation further reveals multiple emission peaks attributed to $Ce^{3+}$, $Sm^{3+}$, $Dy^{3+}$, and $Gd^{3+}$ ions. The composition $CeO_{2-\delta}\cdot(Dy, La, Sm, Y)_2O_3$ exhibited strong emission peaks at 350, 430, and 612 nm that correspond to $^4G_{5/2} \rightarrow {}^6H_J$ transitions of $Sm^{3+}$. Additionally, several weak emissions centered at 344, 420, 443, and 468 nm were observed, associated with the $Ce^{3+}$ ($5d_1 \rightarrow {}^2F_{5/2}$), $Dy^{3+}$ ($^4F_{9/2} \rightarrow {}^6H_{13/2}$), and $Ce^{3+}$ ($5d_2 \rightarrow {}^2F_{7/2}$) transitions were observed, as shown in Figure 10C. These results suggest efficient energy transfer among the rare-earth cations in the HEO matrix. HEO-Gd composition also showed the excitation transition of $Ce^{3+}$, $^2F_{5/2} \rightarrow 5d_1$ at 302 nm. Strong emission peaks at 572, 610, 653, and 718 nm corresponding to $Sm^{3+}$ in $CeO_{2-\delta}\cdot(Gd, La, Sm, Y)_2O_3$ were observed, as shown in Figure 10D. One weak emission centered at 372 nm and corresponding to 4f–4f transition of $Gd^{3+}$ ($^6P_{7/2} \rightarrow {}^8S_{7/2}$) appeared in the spectrum, indicating resonance energy transfer between $Ce^{3+}$ and $Gd^{3+}$.

The PL intensity and bandgap trends are closely tied to oxygen vacancy concentration and structural homogeneity, as evidenced by XPS and UV–Vis data. XPS analysis indicates that oxygen vacancy concentration, calculated from $Ce^{3+}/Ce^{4+}$ and $O_2/O_1$ ratios, is highest in HEO-Gd and HEO-Dy samples sintered for 6 h. The

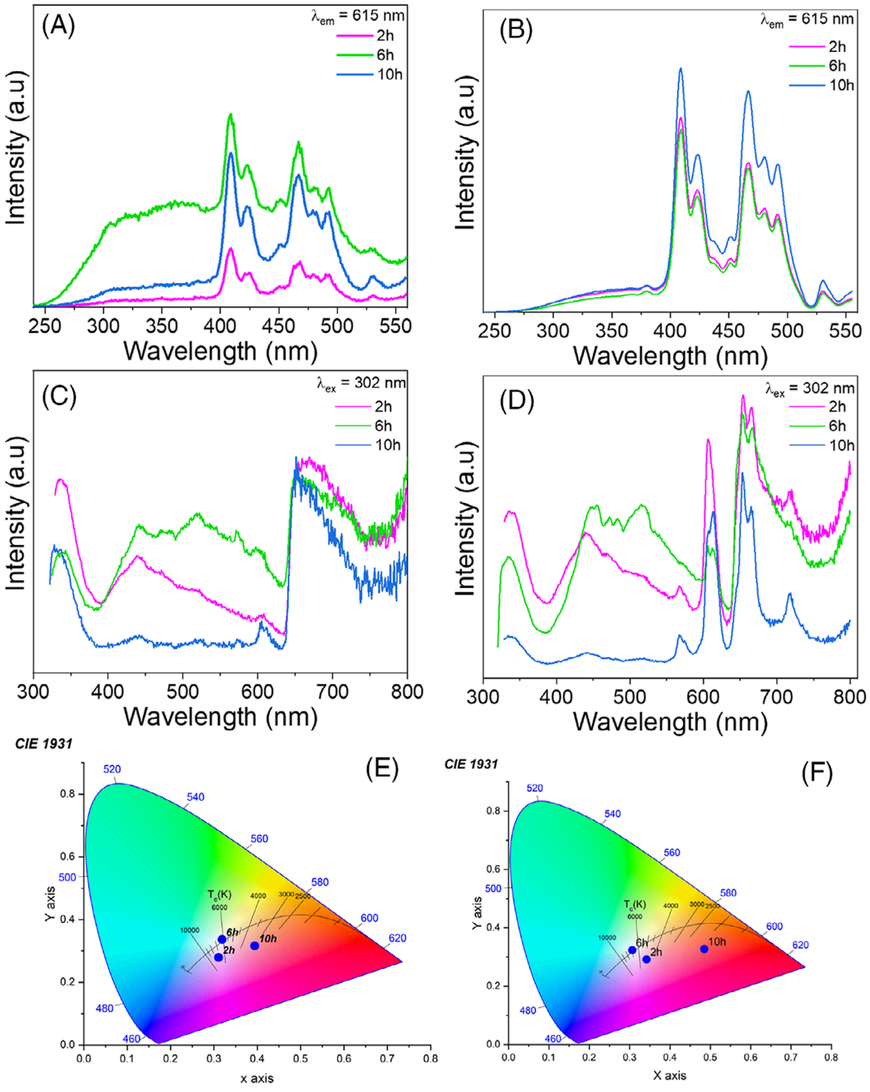

**FIGURE 10** (A and B) Excitation spectra, (C and D) emission spectra of high-entropy oxide (HEO)-Gd and HEO-Dy, and (E and F) Commission International de I' Eclairage France (CIE) chromaticity diagram with 302 nm excitation wavelengths.

samples sintered at 6 h also exhibit the strongest PL intensity, attributed to increased defect-related luminescent centers and a denser, more uniform matrix (>99% relative density) compared to samples sintered for 2 or 10 h.

The optimized sintering conditions promote energy transfer mechanisms, as the denser, more uniform matrix minimizes scattering losses and strengthens ion interactions, boosting emission efficiency.

**TABLE 5** Chromaticity coordinates Commission International de I' Eclairage France (CIE) of high-entropy oxides (HEOs) under 302 nm excitation wavelengths.

| Sample name | Excitation wavelength (nm) | CIE coordinates (x, y) |
|---|---|---|
| HEO-Dy 2 h | 302 | (0.3106, 0.2797) |
| HEO-Dy 6 h | 302 | (0.3187, 0.3366) |
| HEO-Dy 10 h | 302 | (0.3940, 0.3165) |
| HEO-Gd 2 h | 302 | (0.3417, 0.2918) |
| HEO-Gd 6 h | 302 | (0.3064, 0.3233) |
| HEO-Gd 10 h | 302 | (0.4892, 0.3274) |

To assess the visual perception of the PL spectra of $CeO_{2-\delta}\cdot(RE, La, Sm, Y)_2O_3$ (RE = Gd, Dy) ceramics, the Commission International de I' Eclairage France (CIE) 1931 color space system was employed. The emissions spectra were used to calculate the CIE 1931 chromaticity coordinates ($x$, $y$), as illustrated in Figure 10E,F and detailed in Table 5. The CIE diagram provides a widely accepted method for representing all perceivable colors by mixing three primary colors, making it an essential tool for evaluating the color output of luminescent materials. The chromaticity coordinates were derived using the standard tristimulus values ($X$, $Y$, $Z$) following Equation (2):

$$x = \frac{X}{X+Y+Z}, y = \frac{Y}{X+Y+Z} \tag{2}$$

In this chromaticity space, the coordinates ($x$ = 0.33, $y$ = 0.33) represent ideal white light emission. The CIE

**TABLE 6** Luminescence decay lifetimes values of $CeO_{2-\delta}\cdot(RE, La, Sm, Y)_2O_3$ (RE = Gd, Dy) for 2, 6, and 10 h high-entropy oxide (HEO) sample.

| Sample | HEO sample | Average time decay ($\tau_1$) (ns), $\lambda_{exc} = 311$ nm, $\lambda_{em} = 340$ nm | Average time decay ($\tau_2$) (µs), $\lambda_{exc} = 389$ nm, $\lambda_{em} = 510$ nm |
|---|---|---|---|
| $CeO_{2-\delta}\cdot(Dy, La, Sm, Y)_2O_3$ | Dy 2 h | 9.95 | 8.54 |
| | Dy 6 h | 9.96 | 9.73 |
| | Dy 10 h | 10.2 | 8.32 |
| $CeO_{2-\delta}\cdot(Gd, La, Sm, Y)_2O_3$ | Gd 2 h | 9.17 | 7.71 |
| | Gd 6 h | 9.56 | 8.76 |
| | Gd 10 h | 9.37 | 8.48 |

chromaticity diagram illustrates the emitted light characteristics of different HEO compositions under specific excitation wavelengths. The *x*, *y* chromaticity coordinates calculated for $CeO_{2-\delta}\cdot(RE, La, Sm, Y)_2O_3$ (RE = Gd, Dy) composition exhibited near cold white light emission when excited at 302 nm. CIE coordinates confirmed that 6 h sample showed the brightest and most balanced output as the result of structural optimization.

The time-resolved PL decay measurements of $CeO_{2-\delta}\cdot(RE, La, Sm, Y)_2O_3$ (RE = Gd, Dy) HEOs were conducted at the excitation wavelengths of 311 and 389 nm with the emission monitored at 340 and 510 nm. All values are summarized in Table 6. These measurements help to understand the recombination dynamics of charge carriers and the nature of luminescent centers. The presence of two distinct lifetimes confirms the presence of multiple luminescence centers in the HEOs. The fast decay is attributed to $Ce^{3+}$ 5d → 4f transitions, which are dipole allowed and results in rapid radiative recombination. In contrast, the longer lifetime corresponds to the f–f transitions of $Dy^{3+}$ with $Sm^{3+}$ and $Gd^{3+}$ with $Sm^{3+}$ ions, which are parity-forbidden, leading to slower emission due to lower transition probabilities.

The presence of multiple decay components suggests an efficient energy transfer process from $Ce^{3+}$ to $Dy^{3+}/Sm^{3+}$ or $Ce^{3+}$ to $Gd^{3+}/Sm^{3+}$, depending on the compositions. Figure 11A,B confirms that decay curves are well fitted using a triple-exponential function (Equation 3), indicating the presence of multiple recombination pathways that govern the luminescence behavior of these materials.

$$I(t) = A_1 \exp\left(-\frac{t}{\tau_1}\right) + A_2 \exp\left(-\frac{t}{\tau_2}\right) + A_3 \exp\left(-\frac{t}{\tau_3}\right) \tag{3}$$

In the equation, $I$ represent the fluorescence intensity of a phosphor at time $t$ and $A_1$, $A_2$, and $A_3$ are constants. The decay lifetimes are denoted by $\tau_1$, $\tau_2$, and $\tau_3$. The decay curve with triple-exponential mode suggests the existence of three luminescence centers in the phosphor hosts. The average $\tau$ can be calculated according to Equation (4):

$$\tau = \frac{A_1\tau_1^2 + A_2\tau_2^2 + A_3\tau_3^2}{A_1\tau_1 + A_2\tau_2 + A_3\tau_3} \tag{4}$$

The transmittance properties of HEOs with the composition $CeO_{2-\delta}\cdot(RE, Y, Sm, La)_2O_3$ (RE = Dy, Gd), sintered at a dwell time of 6 h, were evaluated to assess their optical clarity for potential applications. After sintering, the ceramic pellets were ground and polished to 1 mm thickness to minimize surface scattering and ensure reliable optical measurement (Figure 11C). Transmittance spectra were recorded using a UV–Vis–NIR spectrophotometer over the wavelength range of 400–1800 nm, as shown in Figure 11D. Both compositions exhibit low transmittance, consistently below 5% across the visible range (400–800 nm) and increasing to ∼20% in the NIR region (800–1800 nm). The image in Figure 11C, showing a polished HEO sample visually confirms the limited optical transmission, and the sample appears semi-opaque with a brownish hue, allowing minimal light transmission.

Despite achieving a high relative density (>99%), which typically enhances translucency, the low transmittance contrasts with expectations for a dense ceramic. This correlates with the oxygen vacancy concentration in 6 h sample, as confirmed by XPS, and with the lowest bandgap and enhanced PL intensity, suggesting increased absorption and reduced transmission in the visible range due to metastable energy states introduced by oxygen vacancies and $Ce^{3+}/Ce^{4+}$ mixed valence.

## 4 | CONCLUSION

HEOs offer promising solutions for advanced optoelectronic and lighting applications. This study aimed to study the influence of processing parameters for the synthesis of dense $CeO_{2-\delta}\cdot(RE, Y, Sm, La)_2O_3$ (RE = Dy, Gd) ceramics on optical properties. HEOs with single-phase cubic bixbyite structure were prepared by reactive sintering at 1600°C for 2, 6, or 10 h. Microstructural and elemental analysis revealed >99% relative density, 2–10 µm grain sizes, and homogeneous element distribution. XPS identified the variation in the concentration of oxygen vacancies in samples sintered with varying dwell times, with 6 h sintered sample showing the highest oxygen vacancy concentration. An increase in oxygen vacancies concentrations after extending the sintering time from 2 to 6 h is caused by internal generation of vacancies due to the presence of mixed oxidations states of cerium. Further increase of the dwell time to 10 h reduces the vacancies

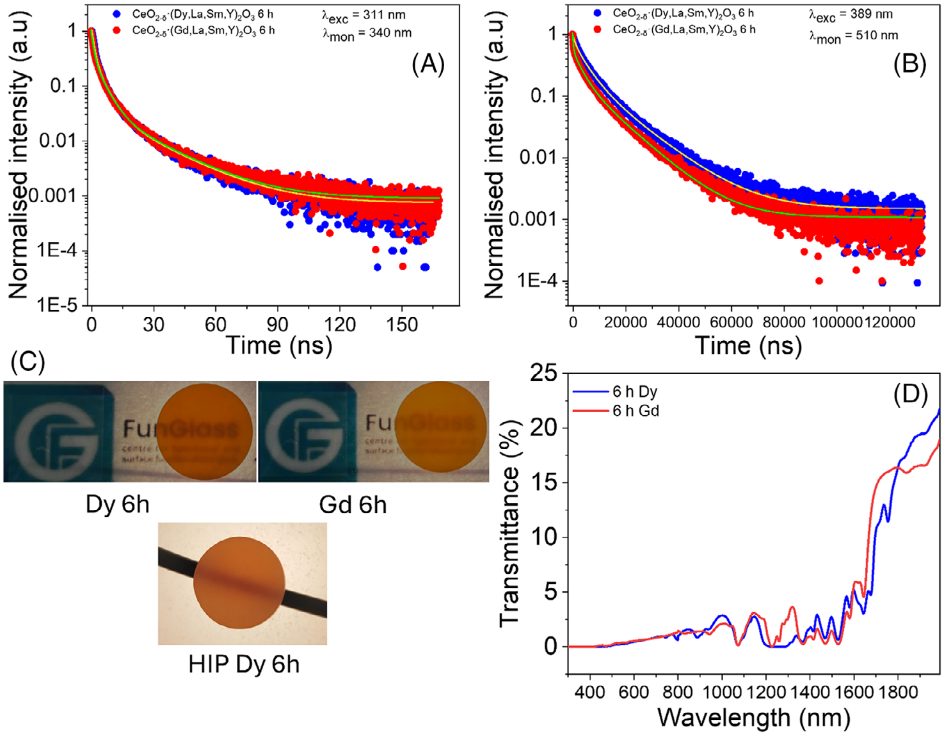

**FIGURE 11** Luminescence decay lifetimes of $CeO_{2-\delta}$·$(RE, La, Sm, Y)_2O_3$ (RE = Gd, Dy) conducted at (A) excitation wavelengths of 311 nm and emission monitored 340 nm and (B) excitation wavelengths of 389 nm and emission monitored at 510 nm. (C) Image of polished samples sintered for 6 h for both compositions and photographs of the Dy sample after hot isostatic pressing (HIP). (D) Transmittance of $CeO_{2-\delta}$·$(RE, Y, Sm, La)_2O_3$ (RE = Dy, Gd) high-entropy oxides (HEOs) sintered for 6 h.

concentration. UV–Vis spectroscopy shows a bandgap reduction in the sample sintered for 6 h, enhancing visible light absorption by oxygen vacancy-induced states that also enhance PL intensity. PL under 302 nm excitation yield blue (432 nm, $Ce^{3+}$), yellow (572 nm, $Sm^{3+}$), and red (653 nm, $Sm^{3+}$) emissions, with the sample sintered for 6 h emitting near-cold white light (CIE; $x = 0.33$, $y = 0.33$) as a result of optimal vacancies concentrations and minimal scattering. Post-sinter HIP impairs transparency due to phase segregation of $Ce_2O_3$.

## ACKNOWLEDGMENTS

Financial support of the grant APVV (23-0424) is gratefully acknowledged.

## ORCID

*Enrico Bernardo* https://orcid.org/0000-0003-4934-4405

*Dušan Galusek* https://orcid.org/0000-0001-5995-8780

## REFERENCES

1. Cao C, Xie A, Zhou T, Zhong H, Lu X, Xie A, et al. $Eu^{3+}$ doped lutetium molybdenum oxides: synthesis, optical properties, thermal behavior, and LED packaging. J Lumin. 2020;217:116759. https://doi.org/10.1016/J.JLUMIN.2019.116759
2. Elkhoshkhany N, Marzouk SY, Khattab MA, Dessouki SA. Influence of $Sm_2O_3$ addition on Judd–Ofelt parameters, thermal and optical properties of the $TeO_2$–$Li_2O$–ZnO–$Nb_2O_5$ glass system. Mater Charact. 2018;144:274–86. https://doi.org/10.1016/J.MATCHAR.2018.07.021
3. Venugopal A, Kaewkhao J, Abhiram J, Rajashekara KM, Rajaramakrishna R, Pramod NG, et al. $Eu^{3+}$ ions doped SrO–CaO–$Li_2O$–$B_2O_3$ glasses for optical display material application. J Phys Conf Ser. 2020;1485(1):012053. https://doi.org/10.1088/1742-6596/1485/1/012053
4. Dai Q, Foley ME, Breshike CJ, Lita A, Strouse GF. Ligand-passivated Eu:$Y_2O_3$ nanocrystals as a phosphor for white light emitting diodes. J Am Chem Soc. 2011;133:10. https://doi.org/10.1021/ja2039419
5. Sarkar A, Wang Q, Schiele A, Chellali MR, Bhattacharya SS, Wang D, et al. High-entropy oxides: fundamental aspects and electrochemical properties. Adv Mater. 2019;31(26):1806236. https://doi.org/10.1002/ADMA.201806236
6. Cheng B, Lou H, Sarkar A, Zeng Z, Zhang F, Chen X, et al. Pressure-induced tuning of lattice distortion in a high-entropy oxide. Commun Chem. 2019;2(1):1–9. https://doi.org/10.1038/s42004-019-0216-2
7. High-entropy materials: theory, experiments, and applications. Springer International Publishing; 2021. https://doi.org/10.1007/978-3-030-77641-1
8. Chen X, Wu Y. High-entropy transparent fluoride laser ceramics. J Am Ceram Soc. 2020;103(2):750–56. https://doi.org/10.1111/JACE.16842
9. Yao Q, Hu P, Sun P, Liu M, Dong R, Chao K, et al. YAG:$Ce^{3+}$ transparent ceramic phosphors brighten the next-generation laser-driven lighting. Adv Mater. 2020;32(19):1907888. https://doi.org/10.1002/ADMA.201907888

10. Hu Z, Xu X, Wang J, Liu P, Li D, Wang X, et al. Fabrication and spectral properties of Dy:$Y_2O_3$ transparent ceramics. J Eur Ceram Soc. 2018;38(4):1981–85. https://doi.org/10.1016/J.JEURCERAMSOC.2017.12.020
11. He Y, Liu K, Xiang B, Zhou C, Zhang L, Liu G, et al. An overview on transparent ceramics with pyrochlore and fluorite structures. J Adv Dielectr. 2020;10(3):20300017. https://doi.org/10.1142/S2010135X20300017
12. Zhang K, Li W, Zeng J, Deng T, Luo B, Zhang H, et al. Preparation of $(La_{0.2}Nd_{0.2}Sm_{0.2}Gd_{0.2}Yb_{0.2})_2Zr_2O_7$ high-entropy transparent ceramic using combustion synthesized nanopowder. J Alloys Compd. 2020;817:153328. https://doi.org/10.1016/J.JALLCOM.2019.153328
13. Zhang G, Milisavljevic I, Zych E, Wu Y. High-entropy sesquioxide $X_2O_3$ upconversion transparent ceramics. Scr Mater. 2020;186:19–23. https://doi.org/10.1016/j.scriptamat.2020.04.011
14. Zhang G, Milisavljevic I, Grzeszkiewicz K, Stachowiak P, Hreniak D, Wu Y. New optical ceramics: high-entropy sesquioxide $X_2O_3$ multi-wavelength emission phosphor transparent ceramics. J Eur Ceram Soc. 2021;41(6):3621–28. https://doi.org/10.1016/J.JEURCERAMSOC.2021.01.027
15. Corey ZJ, Lu P, Zhang G, Sharma Y, Rutherford BX, Dhole S, et al. Structural and optical properties of high entropy (La, Lu, Y, Gd, Ce)$AlO_3$ perovskite thin films. Adv Sci. 2022;9(29):2202671. https://doi.org/10.1002/ADVS.202202671
16. Du M, Xiao Y, Yang X, Ma Y, Han Y, Li Z, et al. High-entropy $(La_{0.2}Dy_{0.2}Er_{0.2}Yb_{0.2}Y_{0.2})_2Zr_2O_7$ oxide, a potential thermal barrier coating material with photoluminescence property sensitive to pressure. Ceram Int. 2024;50(5):8010–16. https://doi.org/10.1016/J.CERAMINT.2023.12.129
17. Li J, Fiato M, Wu Y. Transparent high entropy garnet ceramics by SPS. J Eur Ceram Soc. 2024;44(13):7846–54. https://doi.org/10.1016/J.JEURCERAMSOC.2024.05.063
18. Bai Y, Chai DZ, Shao Y, Zheng C, Li ST, Zhang F, et al. Tuning the p-type conductivity and transparency of perovskite nickelates by configurational entropy. Ceram Int. 2024;50(9):15649–56. https://doi.org/10.1016/J.CERAMINT.2024.02.045
19. Kiryakov A, Kuznetsova Y, Buntov E, Dyachkova T, Murugan J, Chufarov A, et al. High-entropy oxide optical nanoceramics prepared by thermobaric synthesis. J Eur Ceram Soc. 2025;45(9):117316. https://doi.org/10.1016/J.JEURCERAMSOC.2025.117316
20. Chauhan A, Bernardo E, Galusek D. Tailoring optical properties of (Ce, Pr)$O_{2-\delta}$·(La, Sm, Y)$_2O_3$ high entropy oxides by substituting Pr with Gd or Dy for multi-wavelength emission applications. Open Ceram. 2025;21:100730. https://doi.org/10.1016/J.OCERAM.2024.100730
21. Rost CM, Sachet E, Borman T, Moballegh A, Dickey EC, Hou D, et al. Entropy-stabilized oxides. Nat Commun. 2015;6(1):1–8. https://doi.org/10.1038/ncomms9485
22. Gild J, Samiee M, Braun JL, Harrington T, Vega H, Hopkins PE, et al. High-entropy fluorite oxides. J Eur Ceram Soc. 2018;38(10):3578–84. https://doi.org/10.1016/J.JEURCERAMSOC.2018.04.010
23. Song K, Wang S, Sun Q, Xu D. Study of oxidative dehydrogenation of ethylbenzene with $CO_2$ on supported $CeO_2$–$Fe_2O_3$ binary oxides. Arab J Chem. 2020;13(10):7357–69. https://doi.org/10.1016/J.ARABJC.2020.08.013
24. González-Elipe AR, Alvarez R, Holgado JP, Espinos JP, Munuera G, Sanz JM. An XPS study of the $Ar^+$-induced reduction of $Ni^{2+}$ in NiO and Ni–Si oxide systems. Appl Surf Sci. 1991;51(1–2):19–26. https://doi.org/10.1016/0169-4332(91)90058-R
25. Machocki A, Ioannides T, Stasinska B, Gac W, Avgouropoulos G, Delimaris D, et al. Manganese–lanthanum oxides modified with silver for the catalytic combustion of methane. J Catal. 2004;227(2):282–96. https://doi.org/10.1016/J.JCAT.2004.07.022
26. Guo M, Lu J, Wu Y, Wang Y, Luo M. UV and visible Raman studies of oxygen vacancies in rare-earth-doped ceria. Langmuir. 2011;27(7):3872–77. https://doi.org/10.1021/LA200292F
27. De Rouffignac P, Park J, Gordon RG. Atomic layer deposition of $Y_2O_3$ thin films from yttrium Tris(N,N′-diisopropylacetamidinate) and water. Chem Mater. 2005;17(19):4808–14. https://doi.org/10.1021/cm050624+
28. Petrov D. Nanocrystalline $GdAlO_3$: XPS, EPR and magnetic susceptibility studies. Appl Phys A. 2011;104:1237–42. https://doi.org/10.1007/s00339-011-6453-6
29. Hojo H, Mizoguchi T, Ohta H, Findlay SD, Shibata N, Yamamoto T, et al. Atomic structure of a $CeO_2$ grain boundary: the role of oxygen vacancies. Nano Lett. 2010;10(11):4668–72. https://doi.org/10.1021/NL1029336/ASSET/IMAGES/MEDIUM/NL-2010-029336_0003.GIF
30. Estrin Y, Gottstein G, Rabkin E, Shvindlerman LS. On the kinetics of grain growth inhibited by vacancy generation. Scr Mater. 2000;43(2):141–47. https://doi.org/10.1016/S1359-6462(00)00383-3
31. Elmutasim O, Hussien AG, Sharan A, AlKhoori S, Vasiliades MA, Abdelrahman Taha IM, et al. Evolution of oxygen vacancy sites in ceria-based high-entropy oxides and their role in $N_2$ activation. ACS Appl Mater Interfaces. 2023;16:23038–53. https://doi.org/10.1021/ACSAMI.3C16521/ASSET/IMAGES/LARGE/AM3C16521_0015.JPEG
32. Liu Z, Ma H, Sorrell CC, Koshy P, Wang B, Hart JN. Enhancement of light absorption and oxygen vacancy formation in $CeO_2$ by transition metal doping: a DFT study. Appl Catal A Gen. 2024;670:119544. https://doi.org/10.1016/J.APCATA.2023.119544
33. Bagcivan A, Aktas S, Yildirim Y, Polat O, Sobola D, Sen C, et al. Structural and optical evolution in $CeO_2$ films induced by aluminum doping: a comprehensive study. Ceram Int. 2025;51(3):2846–60. https://doi.org/10.1016/J.CERAMINT.2024.11.262
34. Sarkar A, Mannava PK, Velasco L, Das C, Breitung B, Bhattacharya SS, et al. Determining role of individual cations in high entropy oxides: structure and reversible tuning of optical properties. Scr Mater. 2022;207:114273. https://doi.org/10.1016/J.SCRIPTAMAT.2021.114273

**How to cite this article:** Chauhan A, Frickel A, Begand S, Herrmann M, Bernardo E, Galusek D. Highly dense translucent $CeO_{2-\delta}$·(RE, Y, Sm, La)$_2O_3$ (RE = Dy, Gd) high-entropy ceramics for multi-wavelength emission. Int J Appl Ceram Technol. 2025;22:e70047. https://doi.org/10.1111/ijac.70047